A&A 396, 847–855 (2002)
DOI: 10.1051/0004-6361:20021453

Astronomy & Astrophysics

A VLT/FORS2 spectroscopic survey in the HDF-S⋆

E. Vanzella[1,2], S. Cristiani[3,4], S. Arnouts[1], M. Dennefeld[5], A. Fontana[6], A. Grazian[1,2], M. Nonino[3], P. Petitjean[5], and P. Saracco[7]

[1] European Southern Observatory, Karl-Schwarzschild-Str. 2, 85748 Garching, Germany
[2] Dipartimento di Astronomia dell'Università di Padova, Vicolo dell'Osservatorio 2, 35122 Padova, Italy
[3] INAF – Osservatorio Astronomico di Trieste, via G.B. Tiepolo 11, 40131 Trieste, Italy
[4] Space Telescope European Coordinating Facility, Karl-Schwarzschild-Str. 2, 85748 Garching, Germany
[5] Institut d'Astrophysique de Paris, 98bis boulevard Arago, 75014 Paris, France
[6] INAF – Osservatorio Astronomico di Roma, via dell'Osservatorio 2, Monteporzio, Italy
[7] INAF – Osservatorio Astronomico di Brera, via E. Bianchi 46, Merate, Italy

Received 21 June 2002 / Accepted 30 September 2002

Abstract. We report on low-resolution multi-object spectroscopy of 65 objects from $I(AB) \simeq 20$ to $I(AB) \simeq 25$ in the HDF-S obtained with the VLT Focal Reducer/low dispersion Spectrograph (FORS2). 18 objects belong to the HDF-S proper, i.e. the WFPC2 deep area. 15 high-redshift galaxies with $2.0 < z < 3.5$ (10 in the HDF-S proper) have been identified. The spectroscopic redshifts are in good agreement with the photometric ones derived from a χ^2 minimization technique comparing the observed spectral energy distribution with synthetic libraries and with a new neural network (*NN*) approach. The dispersion with the former method is $\sigma_z = 0.16$ whereas the latter provides $\sigma_z = 0.13$. No "catastrophic" difference is encountered. The inferred star formation rates of the individual objects range from tens to a few hundreds of $M_\odot$ yr^{-1} and the global star formation rate of the Universe at $< z > \simeq 2.4$ is estimated to be 0.15 $M_\odot$ yr^{-1} Mpc^{-3} with a statistical error of 0.04.
Evidence for large-scale structure is found with two groups' redshifts observed at $z \simeq 2.1$ and $z \simeq 2.7$ and a pronounced low redshift peak around $z \simeq 0.58$.
An elliptical galaxy lensing a background object turns out to be at a redshift $z = 0.577$.

Key words. techniques: spectroscopic – galaxies: evolution – galaxies: formation – galaxies: distances and redshifts

1. Introduction

The Hubble Deep Field South (HDF-S) is a region of intense astrophysical interest. A large set of observations of an otherwise unremarkable field around the QSO J2233-606 ($z = 2.24$) has been taken in parallel by three instruments aboard the Hubble Space Telescope (HST): the Wide Field and Planetary Camera 2 (WFPC2), the Space Telescope Imaging Spectrograph (STIS) and the Near Infrared Camera and Multi-Object Spectrometer (NICMOS). This unique database has been complemented with a vigorous campaign of ground-based observations from the optical to the radio by virtually all the major observatories in the southern hemisphere.

In a series of papers we have presented deep near-IR observations of the HDF-S (Saracco et al. 2001), a multicolor (U, B, V, I, Js, H, Ks) catalog in the WFPC2 area (Vanzella et al. 2001), preliminary spectroscopic identifications (Cristiani et al. 2000), photometric redshifts (Fontana et al. 2002; Vanzella et al. in preparation), studies of the redshift distribution and evolution of the galaxy luminosity function (Fontana et al. 1999; Fontana et al. 2000; Poli et al. 2001) and clustering (Arnouts et al. 2002), as well as high-resolution spectroscopy of the HDF-S QSO J2233-606 (Cristiani & D'Odorico 2000).

In the present paper we report the results of a spectroscopic campaign aiming at the confirmation of all the high-redshift galaxy candidates in the WFPC2 area brighter than $I(AB) = 24.25$. A cosmology with $H_0 = 70$ km s^{-1} Mpc^{-1}, $\Omega_M = 0.3$ and $\Omega_\Lambda = 0.7$ is assumed throughout.

2. The photometric databases and the selection of the candidates

Deep multicolor imaging of the HDF-S has been obtained from the space and from the ground. In particular the WFPC2 data, consisting of deep images in the F300W, F450W, F606W and F814W filters, cover an area of 4.7 sq arcmin reaching 10σ AB magnitude limits of 26.8, 27.7, 28.2 and 27.7 (in a 0.2 sq arcsec area). *UBVRIJHK* data over an area of 25 sq arcmin, including the WFPC2 field, have been obtained at the ESO 3.5 m New Technology Telescope (NTT) as a part of the ESO Imaging Survey (EIS) program (da Costa et al. 1998). They reach 2σ limiting magnitudes of $U_{AB} \sim 27$, $B_{AB} \sim 26.5$, $V_{AB} \sim 26$, $R_{AB} \sim 26$, $I_{AB} \sim 25$, $J_{AB} \sim 25$, $H_{AB} \sim 24$ and $K_{AB} \sim 24$, in $2 \times FWHM$ diameter apertures. Near infrared images centered in the WFPC2 field have been obtained with

Send offprint requests to: E. Vanzella, e-mail: evanzell@eso.org
⋆ Based on observations collected at the European Southern Observatory, Paranal, Chile.

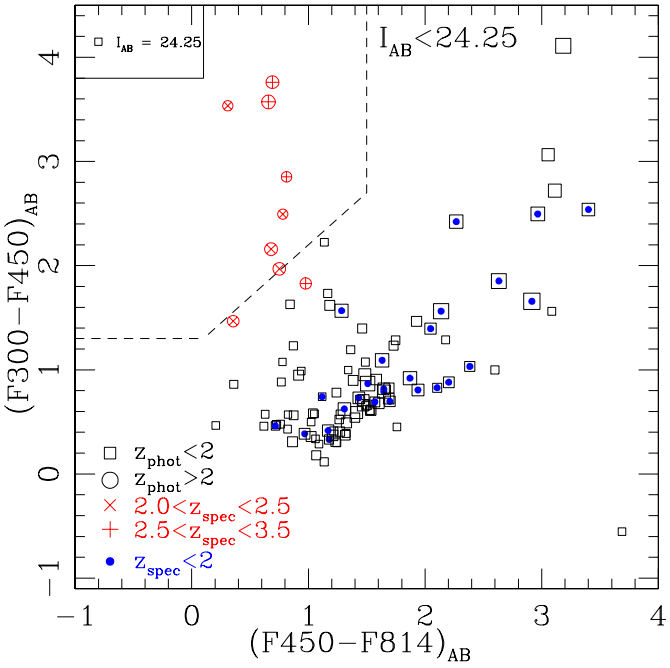

Fig. 1. Selection of the high redshift galaxies (*U* band *dropout*). The dashed line outlines the two-color selection criterion. The size of the symbols is inversely proportional to the magnitude of the objects.

the ISAAC instrument at the VLT in the filters *J*s, *H* and *K*s. A first set of observations, obtained in 1999, have been published by Saracco et al. (2001) and reach the *AB*-magnitude 24.4, 23.5, 24.0 in the *J*s, *H* and *K*s band respectively, at 5σ in a $2 \times FWHM$ diameter aperture. The photometric catalog is described in Vanzella et al. (2001). The final set with the complete reduction is currently being analyzed and reaches 25.0, 24.0, 24.5 in the *J*s, *H* and *K*s band, respectively.

3. Spectroscopic observations

The main emphasis of the present work is on high-redshift galaxies.

In the HDF-S proper, i.e. in the WFPC2 deep area, high redshift ($z \geq 2$) galaxy candidates were selected on the basis of two-color diagrams F300-F450 vs. F450-F814, see Fig. 1. Spectroscopic observations of the nine high-z galaxy candidates with $I(AB) < 24.25$ have been carried out, confirming all of them to be galaxies with $2 < z < 3.5$.

Outside the WFPC2 field, targets were selected from a list of Lyman-break candidates produced by the EIS project [astro-ph/9812105].

The present spectroscopic observations were carried out with the FORS2 instrument (Nicklas et al. 1997) in multiple object spectroscopy (MOS) mode on September 2000.

In the FORS2 MOS mode, 19 pairs of movable slit blades can be placed in a FOV of 6.8×6.8 sq arcmin. The actual useful field in the direction of the dispersion is somewhat smaller and depends on the length of the spectra/dispersion. In the present case the grism I150 was used, providing a useful field of 3.5×6.8 sq arcmin. The journal of the observations is given in Table 1. Three different pointings were observed.

Table 1. Journal of the MOS Observations.

Field	α_{2000}	δ_{2000}	date	exp.time (ks)
A	22:32:54	−60:33:54	2000-Sep.-1	$4 \times 2.7 + 2.4$
B	22:32:51	−60:34:14	2000-Sep.-2	4×3.6
D	22:32:54	−60:33:54	2000-Sep.-2	$4 \times 3.6 + 1.2$

In the choice of the objects to be observed, priority was given to high redshift galaxy candidates with $I(AB) < 24.25$. When no suitable candidate was available for the allowed range of positions of a given slit, a random object in the field was chosen. In a number of cases more than one object was placed in a given slit and/or the position of the slit was changed from one exposure to another of a given pointing. In this way the final number of obtained spectra exceeds 19 per pointing.

The MOS observations were reduced with the MIDAS package, using commands of the LONG and MOS contexts. For each object the available 2-D spectra were stacked and then an optimal extraction was carried out. The resulting spectroscopic identifications are listed in Table 2 and the spectra of the 15 galaxies with redshifts larger than 2 are shown in Figs. 2 and 3.

The photometric data of Table 2 Col. 5 have been taken from the multicolor catalog of the HDF-S produced by Vanzella et al. (2001).

Figure 4 shows the magnitude distribution (upper panel) and the redshift distribution (lower panel) for the spectroscopic sample in the WFPC2, including previous observation in the literature (Glazebrook et al. http://www.aao.gov.au/hdfs/Redshifts/; Cristiani et al. 2000; Rigopoulou et al. 2000; Franceschini et al. 2002). It is worth to note that the spectroscopic sample is 100% complete down to $I_{AB} \simeq 21$, and 75% down to $I_{AB} \simeq 22.5$.

The behavior of the redshift distribution shows an evident peak at redshift $z \simeq 0.58$, indicating the presence of large scale structure, (see also, Dennefeld 2001). More details will be discussed in a forthcoming paper (Dennefeld et al. in preparation).

4. Reliability of the photometric redshift

The present observations, together with previously published data (Glazebrook et al. http://www.aao.gov.au/hdfs/Redshifts/; Cristiani et al. 2000; Rigopoulou et al. 2000; Franceschini et al. 2002) provide 46 spectroscopic identifications in the WFPC2 area, the full list is given in Table 3. Eight objects, marked with a colon (:) in Col. 1, have unreliable photometry (they are near the border of the WF camera).

Photometric redshifts in the WFPC2 field have been computed adopting two techniques. The first method is based on a χ^2 minimization comparing the observed magnitudes (SED) with synthetic libraries (Arnouts et al. 2002; Fontana et al. 2000). Figure 5 shows the comparison between photometric and spectroscopic redshifts for the sample available in the WFPC2 field using the GISSEL00 version of the package by Bruzual & Charlot (1993). Objects with unreliable photometry

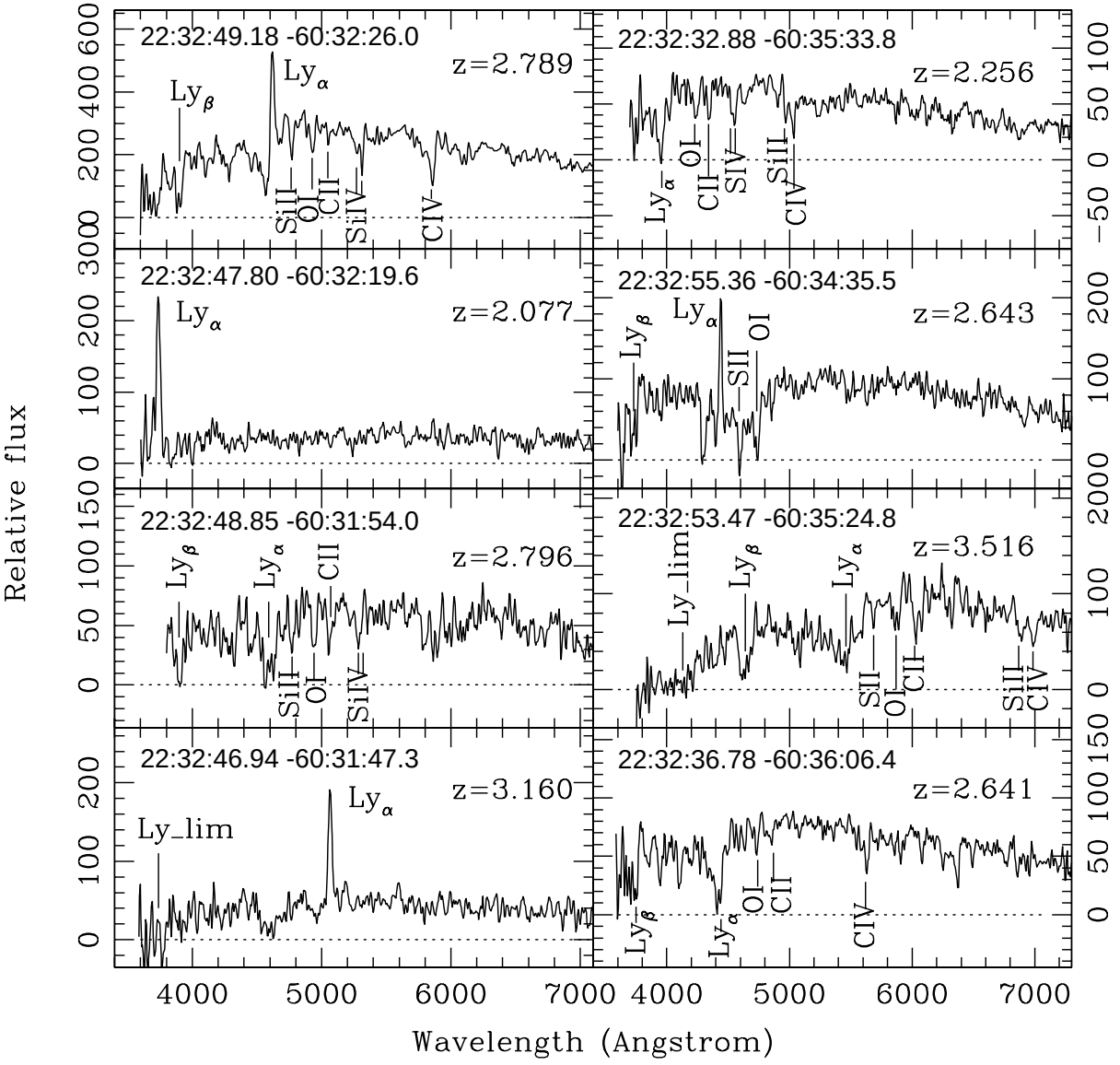

Fig. 2. Spectra of 8 high-redshift galaxies observed in the HDF-S. The ordinate gives the relative flux density per Angstrom. The identification numbers in the upper left of the panels provide the RA and declination for each target.

have not been considered. More details will be discussed in a companion paper (Fontana et al. 2002).

The second method is based on a neural network (*NN*) approach (Vanzella et al. in preparation). Figure 6 shows the results of the prediction on the spectroscopic sample of the HDF-S. The network used is the classical *multilayer perceptron* (MLP) with the standard *backpropagation* learning algorithm (for an introduction to artificial neural networks see C.A.L. Bailer-Jones et al. [astro-ph/0102224]).

The *backpropagation* has been used to train the MLP on the available spectroscopic sample in the HDF-N (Cohen et al. 2000) mixed with a set of SEDs computed from the templates of Coleman et al. (1980).

After a suitable training, based on a bootstrap technique, the *NN*s have been applied to the HDF-S spectroscopic sample.

A *NN* with different architecture has been used as a binary classifier to divide the sources into the two classes of high ($z > 1.75$) and low ($z < 1.75$) redshift, corresponding to 1. and 0. respectively (upper panel of Fig. 6). The classification is correct for all the spectroscopically identified objects. The input pattern in this case contains the colors, the apparent luminosity in the *I* band and the isophotal area of the object (obtained on the basis of the SExtractor package, Bertin & Arnouts 1996).

The middle panel of Fig. 6 shows the direct evaluation of the redshift for the same sample. In this case the input pattern consists of the colors.

The two methods have produced a similar dispersion, $\sigma_z \simeq 0.13$ for the neural approach and $\sigma_z \simeq 0.16$ for the χ^2 minimization technique, in a sample where the objects with unreliable photometry are not included (38 galaxies). Including also these objects the neural approach gives again $\sigma_z \simeq 0.13$.

The general agreement of the photometric redshifts with the observed ones is remarkable. It should be noted, however, that the high-redshift galaxy candidates have been selected on

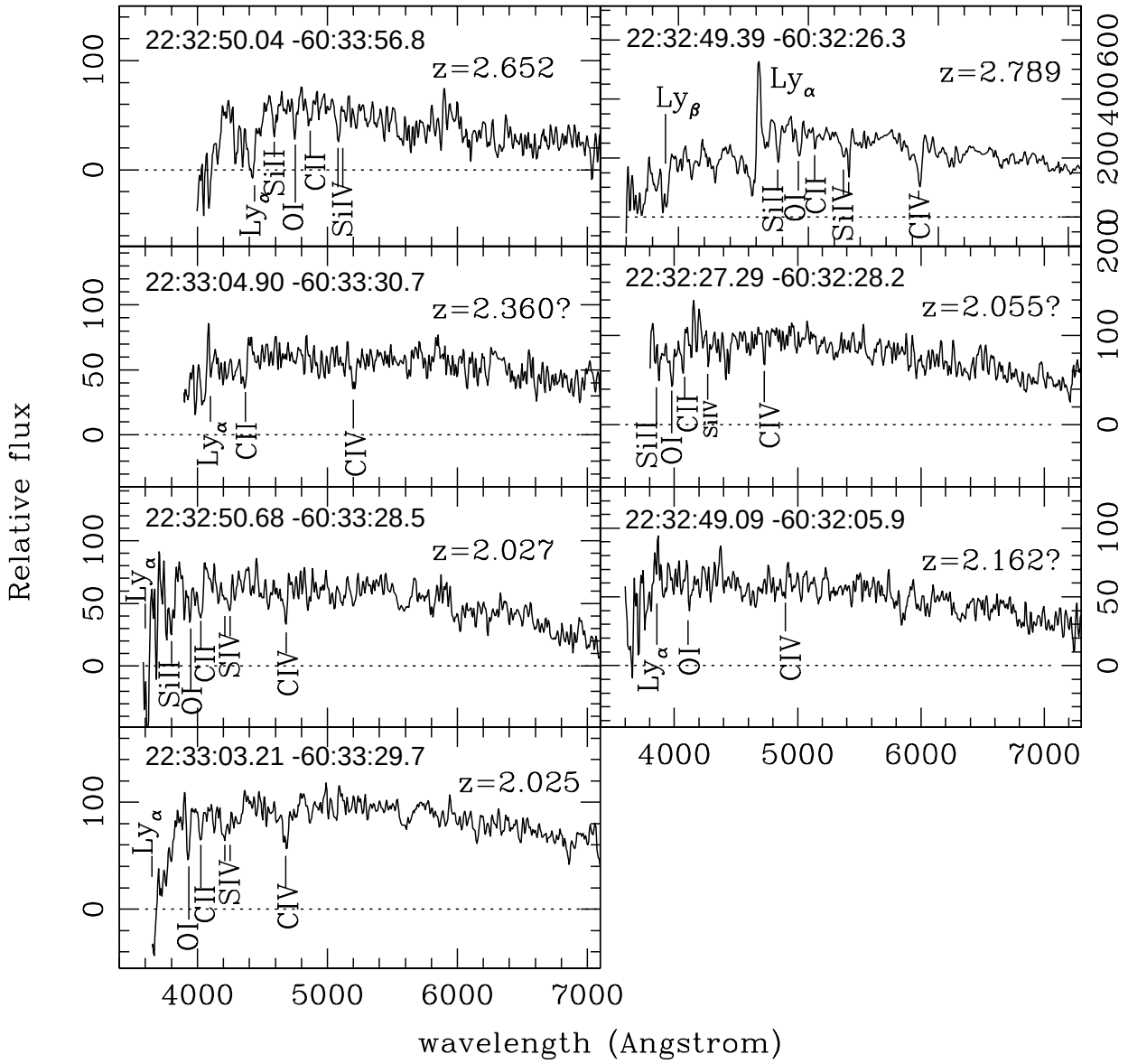

Fig. 3. Spectra of 7 high-redshift galaxies observed in the HDF-S. The ordinate gives the relative flux density per Angstrom. The identification numbers in the upper left of the panels provide the RA and declination for each target.

the basis of color criteria, which are not entirely independent of the photometric redshift approach. For example, if there are galaxies truly at high redshift with peculiar colors that the photometric redshift technique would predict to be at low-z, they might not have been selected with the color criteria described in Sect. 2, biasing the measured scatter in redshift.

5. High redshift galaxies

In this spectroscopic survey 15 high redshift galaxies ($z > 2$) have been identified (9 are inside the WFPC2 area and one is near its border).

A $F300 - F450$ vs. $F450 - F814$ diagram of the objects in the WFPC2 area with $I(AB) < 24.25$ is shown in Fig. 1. Such a plot is customarily used to find high redshift galaxies and in the present case 7 galaxies with $z > 2$ have been selected according to a standard color criterion (Madau et al. 1996). The photometric redshift techniques make it possible to increase the completeness of the sample, leading to the selection of two more galaxies with $z > 2$.

The redshift distributions of high redshift galaxies ($2 < z < 3.5$) in the HDF-N and HDF-S with $I(AB) < 24.25$ are shown in Fig. 7. Two groups of redshift are apparent in the HDF-S around $z \simeq 2.1$ (4 galaxies) and $z \simeq 2.7$ (4 galaxies). The KS test excludes at the 2% level the hypothesis that (neglecting any selection function) the distribution of redshift in the HDF-S is uniform between $z = 2$ and $z = 3.5$.

The comparison with the HDF-N spectroscopic sample at the same magnitude limit gives a KS probability less than 10% that the two samples are drawn from the same parent population.

It is interesting to note that the galaxy HDF-S 1432 ($z = 2.077$) has the same redshift as a metal absorption system at $z = 2.07728$ identified by Cristiani & D'Odorico (2000) in

Table 2. Spectroscopic identifications in the HDF-S.

N_{obj}	α_{2000}	δ_{2000}	z	I_{AB}	ID
1	22:32:20.22	−60:32:05.5	0.669	–	–
2	22:32:23.04	−60:32:14.0	0.5125	–	–
3	22:32:27.29	−60:32:28.2	2.055?	–	–
4	22:32:30.81	−60:32:47.7	0.579	–	–
5	22:32:32.88	−60:35:33.8	2.256	–	–
6	22:32:33.40	−60:36:59.7	0.3704	–	–
7	22:32:35.75	−60:36:22.4	0.4727	–	–
8	22:32:36.40	−60:35:18.2	0.3678	–	–
9	22:32:36.68	−60:36:57.2	0.5153	–	–
10	22:32:36.78	−60:36:06.4	2.641	–	–
11	22:32:36.94	−60:35:13.0	0.4209	–	–
12	22:32:37.34	−60:31:57.6	1.214?	–	–
13	22:32:38.37	−60:36:49.6	star	–	–
14	22:32:39.00	−60:36:32.0	0.7567	–	–
15	22:32:39.67	−60:34:44.7	0.425	–	–
16	22:32:40.63	−60:34:47.0	0.277	–	–
17	22:32:41.20	−60:35:41.2	0.4138	–	–
18	22:32:42.15	−60:37:14.5	0.3000	–	–
19	22:32:44.35	−60:31:11.5	0.5146	–	–
20	22:32:44.91	−60:30:55.5	0.5125	–	–
21	22:32:45.60	−60:34:18.7	0.4594	–	–
22	22:32:45.68	−60:36:55.5	0.5256	–	–
23	22:32:46.94	−60:31:47.3	3.160	–	1527
24	22:32:47.80	−60:32:19.6	2.077	24.22	1432
25	22:32:48.84	−60:32:03.6	–	24.09	1314
26	22:32:48.85	−60:31:54.0	2.796	23.80	1312
27	22:32:49.09	−60:32:05.9	2.162?	23.75	1284
28	22:32:49.18	−60:32:26.0	2.789	23.28	1277
29	22:32:49.39	−60:32:26.3	2.789	22.92	1242
30	22:32:50.00	−60:33:45.1	–	23.63	1178
31	22:32:50.04	−60:33:56.8	2.652	24.14	1174
32	22:32:50.47	−60:30:36.1	star	–	–
33	22:32:50.51	−60:31:03.0	0.5959	–	–
34	22:32:50.68	−60:33:28.5	2.027	23.32	1100
35	22:32:50.70	−60:33:25.9	1.1369	24.00	1098
36	22:32:50.73	−60:33:26.2	1.1369	24.68	1095
37	22:32:50.90	−60:32:43.0	0.5776	20.90	1088
38	22:32:50.90	−60:32:43.0	–	24.79†	arc
39	22:32:50.95	−60:43:15.4	–	24.07	1074
40	22:32:51.10	−60:34:08.2	–	23.53	1053
41	22:32:51.12	−60:34:08.0	0.1798	–	–
42	22:32:51.17	−60:32:34.0	–	24.28	1061
43	22:32:52.06	−60:31:40.8	0.5116	22.60	973
44	22:32:53.47	−60:35:24.8	3.5161	–	–
45	22:32:53.85	−60:32:13.1	–	23.86	771
46	22:32:53.92	−60:33:13.5	0.3645	21.08	758
47	22:32:54.02	−60:33:05.6	0.5804?	22.74	746
48	22:32:54.09	−60:31:42.7	0.512	22.76	751
49	22:32:54.80	−60:31:13.9	0.546	–	–
50	22:32:54.81	−60:31:13.9	0.512	–	–
51	22:32:54.82	−60:31:31.2	0.513	–	–
52	22:32:55.36	−60:34:35.5	2.643	–	–
53	22:32:55.65	−60:31:16.8	0.5112	–	–

† Magnitude in Vega system, from Barkana et al. (2000).

Table 2. Spectroscopic identifications in the HDF-S (continued).

N_{obj}	α_{2000}	δ_{2000}	z	I_{AB}	ID
54	22:32:56.20	−60:31:07.9	0.5108	–	–
55	22:32:57.72	−60:34:08.6	Mstar	23.05	427
56	22:32:58.60	−60:33:46.6	–	25.75	373
57	22:32:59.78	−60:35:15.7	Mstar	–	–
58	22:33:03.21	−60:33:29.7	2.025	23.25	115
59	22:33:03.86	−60:33:08.8	0.970	22.98	86
60	22:33:04.90	−60:33:30.7	2.360?	24.20	28
61	22:33:05.79	−60:34:36.8	0.564	–	–
62	22:33:06.17	−60:30:44.3	Mstar	–	–
63	22:33:06.19	−60:30:56.2	star	–	–
64	22:33:09.53	−60:34:36.2	1.160	–	–
65	22:33:12.65	−60:33:50.1	Mstar	–	–

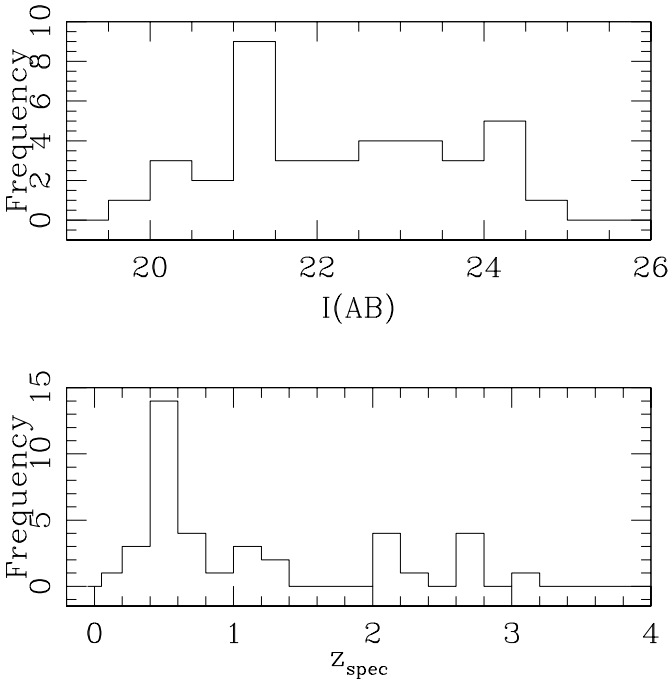

Fig. 4. In the upper panel the magnitude distribution is shown. In the lower panel the redshift distribution is shown. In both cases for the spectroscopic sample in the WFPC2, including the previous observations (see text).

the spectrum of the HDF-S QSO J2233-606. The system shows at least two components and the CIV λ1548−1550 doublet, SiII λ1260, SiIII λ1206 and FeII λ2382 transitions are observed in addition to a strong $\log(N_{\rm HI}) > 15$ Lyα. Coincidences of absorption systems on scales up to several arcminutes (D'Odorico et al. 2002) are observed in the spectra of quasars as the signature of spatial correlation of high density peaks. In the present case the distance between the galaxy HDF-S 1432 and the absorber, 6.2 arcmin, corresponds to 3.1 proper Mpc and is suggestive of a large scale structure at $z \sim 2$, which would be extremely interesting to further investigate by carrying out the identification of Lyman-break galaxies in correspondence of the HDF-S STIS field.

Table 3. Spectroscopic redshifts of objects in the WFPC2 HDF-S field.

ID	α_{2000}	δ_{2000}	z	I_{AB}	ref.
1527:	22:32:46.94	−60:31:47.3	3.160	–	1
1440:	22:32:47.57	−60:34:08.6	0.560	21.22	2
1435	22:32:47.66	−60:33:35.9	0.580	19.53	3
1432	22:32:47.80	−60:32:19.6	2.077	24.22	1
1312	22:32:48.85	−60:31:54.0	2.796	23.80	1
1309	22:32:48.88	−60:32:16.1	0.580	22.96	4
1284	22:32:49.09	−60:32:05.9	2.162?	23.75	1
1277	22:32:49.18	−60:32:26.0	2.789	23.28	1
1242	22:32:49.39	−60:32:26.3	2.789	22.92	1
1178	22:32:50.00	−60:33:45.2	1.152	23.63	1
1174	22:32:50.04	−60:33:56.8	2.652	24.14	1
1160	22:32:50.29	−60:32:03.3	0.414	22.23	4
1100	22:32:50.68	−60:33:28.5	2.027	23.32	1
1098	22:32:50.70	−60:33:25.9	1.137	24.00	1
1095	22:32:50.73	−60:33:26.2	1.137	24.68	1
1088	22:32:50.90	−60:32:43.0	0.579	20.90	1
1015	22:32:51.51	−60:33:37.6	0.577	22.12	4
973:	22:32:52.06	−60:31:40.8	0.512	22.60	1
948	22:32:52.14	−60:33:59.6	0.564	21.79	4
936	22:32:52.24	−60:34:02.8	0.511	22.11	4
935	22:32:52.30	−60:33:08.5	0.583	21.09	4
853	22:32:53.03	−60:33:28.5	1.270	22.60	2
820	22:32:53.33	−60:32:39.3	1.114	22.46	4
790	22:32:53.64	−60:32:36.0	0.365	21.15	4
789	22:32:53.70	−60:32:06.2	1.116	23.29	4
775	22:32:53.74	−60:33:37.6	0.565	21.48	4
758	22:32:53.92	−60:33:13.5	0.364	21.08	1
746	22:32:54.02	−60:33:05.6	0.580?	22.74	1
743	22:32:54.05	−60:32:51.7	0.515	22.14	4
751:	22:32:54.09	−60:31:42.7	0.512	22.76	1
667	22:32:54.68	−60:33:33.2	0.173	21.25	4
592	22:32:55.72	−60:32:11.5	0.673	21.59	4
562	22:32:56.07	−60:31:48.9	0.514	21.24	4
443	22:32:57.54	−60:33:06.1	0.583	20.46	3
434:	22:32:57.75	−60:32:33.0	0.517	22.00	4
420:	22:32:57.99	−60:32:34.3	0.760	21.34	2
402	22:32:58.22	−60:33:31.6	0.423	21.98	4
257	22:33:00.15	−60:33:19.0	0.540	23.22	3
254:	22:33:00.24	−60:32:33.9	0.415	20.58	4
182	22:33:01.77	−60:34:13.5	1.230	22.43	2
154	22:33:02.45	−60:33:46.5	0.696	22.29	3
141	22:33:02.76	−60:33:22.1	0.465	20.31	4
115	22:33:03.21	−60:33:29.7	2.025	23.25	1
98	22:33:03.57	−60:33:41.7	0.340	20.07	4
86:	22:33:03.86	−60:33:08.8	0.970	22.98	1
28	22:33:04.90	−60:33:30.7	2.360?	24.20	1

1) This work.
2) Franceschini et al. (in preparation).
3) `http://www.aao.gov.au/hdfs/Redshifts`
4) Dennefeld et al. (in preparation).

A bright pair ($I(AB) = 23.28, 22.92$ and $ID = 1277, 1242$ respectively) of interacting galaxies has been identified at redshift 2.789. The angular separation is 1.76″, corresponding to a proper separation of 13.8 kpc.

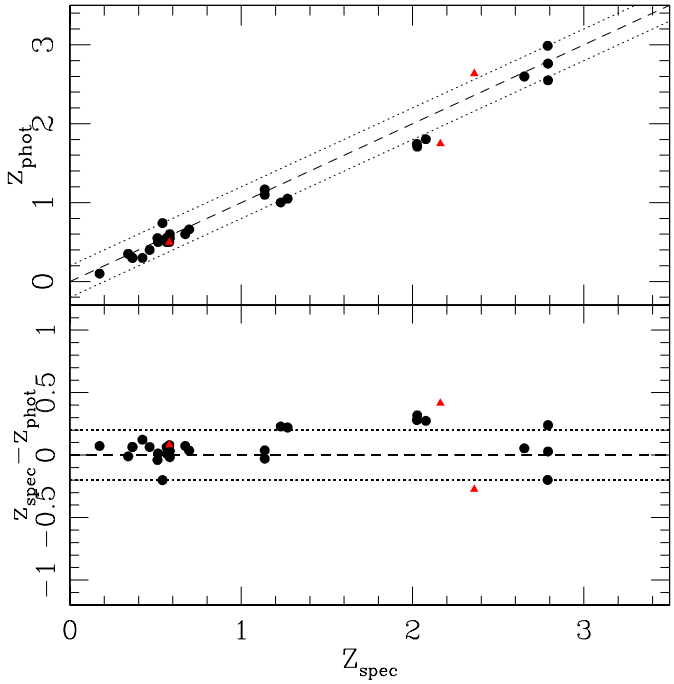

Fig. 5. Predictions with the χ^2 minimization technique in the HDF-S spectroscopic sample. Objects with the unreliable photometry have not been considered. The triangles represent the uncertain spectroscopic redshifts.

Figure 8 shows the morphology of each high redshift galaxy in the optical (WFPC2) and near infrared bands.

The properties of the high-z galaxies confirmed with the present observations are summarized in Table 4. They have been inferred from the GISSEL models best-fitting the photometric data (Arnouts et al. 1999), imposing the redshift at the spectroscopic value and assuming a continuous star formation. Columns 4–7 list the estimated star formation rate (SFR), age, stellar mass and E_{B-V} extinction, respectively.

Column 8 lists the SFR empirically derived from the photometry and corrected for the intrinsic absorption according to the calibration of Meurer et al. (1999). The UV slope, β, of the SED is estimated on the basis of the $V-I$ color and the redshift with the relation

$$\beta = 3.23(V_{606} - I_{814})_{\rm AB} - 5.22 + 2.66z - 0.545z^2 \quad (1)$$

and the absorption at 160 nm A_{1600} is obtained using the conversion:

$$A_{1600} = 4.43 + 1.99\beta. \quad (2)$$

The Calzetti extinction law (Calzetti 1997) has been adopted to estimate the empirical E_{B-V} (Col. 9) from A_{1600}. For a Salpeter IMF ($0.1\ M_\odot < M < 100\ M_\odot$) with constant SFR, a galaxy with SFR = 1 $M_\odot$ yr $^{-1}$ produces $L(160\ {\rm nm}) = 9.19 \times 10^{39}$ erg s^{-1} Å^{-1} (Meurer et al. 1999). The inferred star formation rates in the present sample range from a few tens to few hundred $M_\odot$ yr^{-1}.

By summing all the SFRs of Col. 4, we obtain an estimate for the global star formation rate of the Universe of 0.056 $M_\odot$ yr^{-1} Mpc^{-3} at $< z > \simeq 2.4$. The completeness

Table 4. Properties of the Galaxies with $z > 2$ in the HDF-S field.

ID	$I(AB)$	$z_{\rm spec}$	$SFR(GIS)$ ($M_\odot$ yr^{-1})	AGE (Gyr)	MASS $\left[\mathrm{Log}\left(\frac{M_\star}{M_\odot}\right)\right]$	$E_{B-V}(GIS)$ (mag)	SFR(emp) ($M_\odot$ yr^{-1})	E_{B-V}(emp) (mag)
1100	23.32	2.027	86	0.40	10.54	0.30	132	0.26
115	23.25	2.025	97	0.20	10.29	0.30	124	0.24
1432	24.22	2.077	39	0.51	10.30	0.30	70	0.28
1284	23.75	2.162	23	0.32	9.87	0.15	47	0.15
28	24.20	2.360	22	0.05	9.05	0.15	28	0.10
1174	24.14	2.652	66	0.04	9.42	0.25	86	0.21
1242	22.92	2.789	211	0.01	9.34	0.20	188	0.16
1277	23.28	2.789	60	0.20	10.08	0.15	124	0.14
1312	23.80	2.796	52	0.51	10.42	0.20	95	0.17

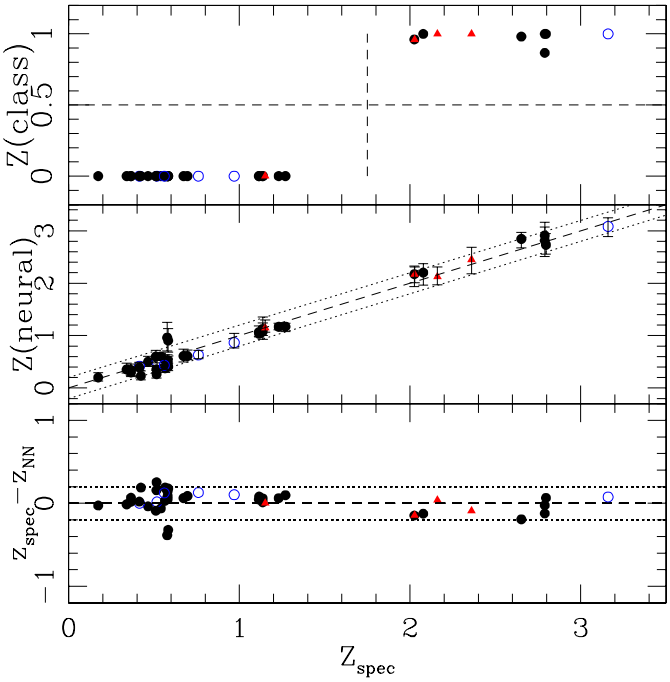

Fig. 6. Predictions with the neural network approach in the HDF-S spectroscopic sample. In the upper panel the classification between low and high redshift galaxies, less than 1.75 and greater than 1.75, respectively. In the middle and lower panels the comparison between neural photometric redshifts and the spectroscopic ones. Open circles represent objects with unreliable photometry and triangles are objects with uncertain spectroscopic redshift.

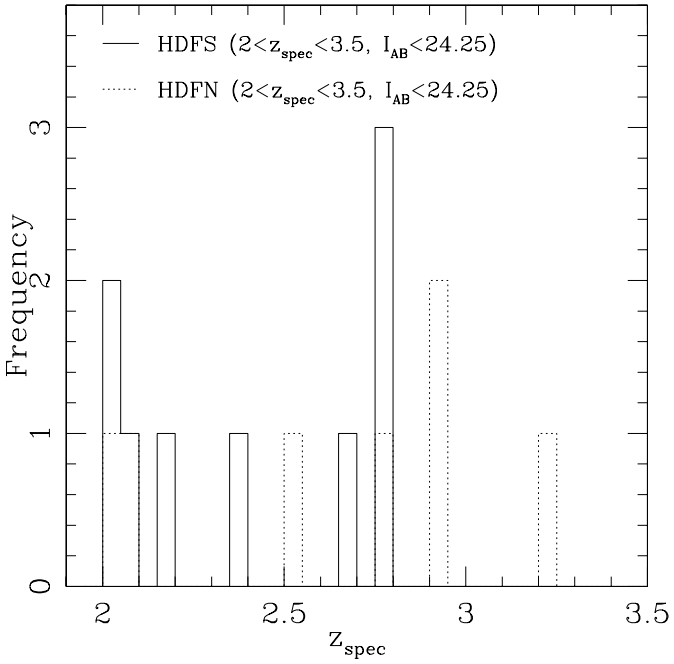

Fig. 7. Comparison between high redshift galaxies distributions in the HDF-S (solid line) and HDF-N (dotted line) with at $I_{AB} < 24.25$ and $2 < z < 3.5$.

limit of the present sample, $I_{AB} = 24.25$ corresponds to a $M_{1700} = -20.47 = M_\star + 0.37$ (assuming a typical $V - I = 0.25$ for our Lyman break galaxies), where $M_\star = -20.84$ at 1700 Å is derived from Poli et al. (2001). Integrating over the whole luminosity range of the luminosity function a correction factor of 2.7 is readily obtained, corresponding to an estimate for the universal SFR of 0.15 ± 0.04 $M_\odot$ yr^{-1} Mpc^{-3}. This is in good agreement with recent estimates in the literature as shown in Fig. 9. The same procedure carried out on the HDF-N (Cohen et al. 2000; Fernández-Soto et al. 1999) down to $I_{AB} = 25.35$ provides an estimate for the universal SFR of 0.11 ± 0.03 $M_\odot$ yr^{-1} Mpc^{-3} at a median redshift of 2.8.

6. Individual notes

An evident gravitational lensing effect is present in the HDF-S field. The system consists of an arc at a radius of 0.9″ around an elliptical galaxy (Barkana et al. 2000). We have obtained a spectrum of the lensing galaxy ($ID = 1088$, $N_{\rm obj} = 37$), which turns out to be an elliptical at redshift 0.577 (see also Dennefeld 2001). In this way the results obtained by Barkana et al. assuming $z_{\rm phot} \simeq 0.6$ for the lensing galaxy are confirmed.

We have also tried to obtain a redshift for the arc by comparing two spectra taken at different position angles.

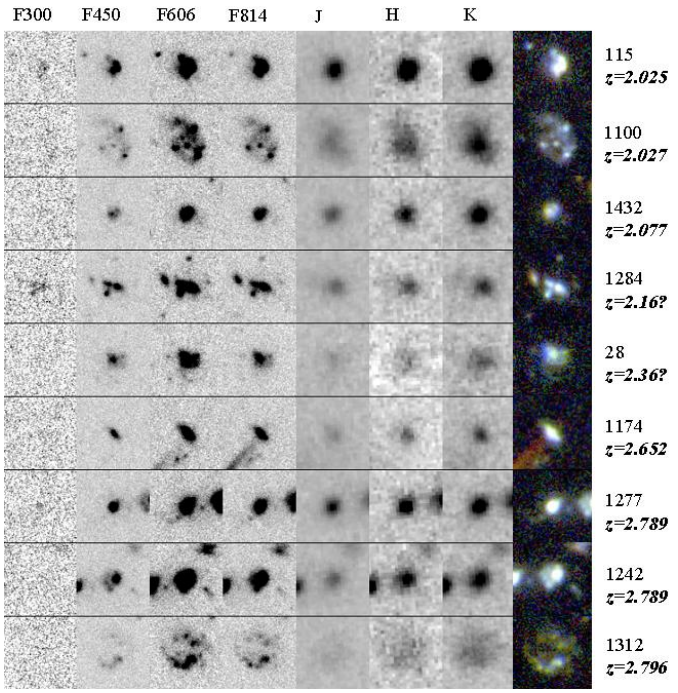

Fig. 8. High redshift galaxies in the seven bands and color composition. The side of each box is 3.5 arcsec.

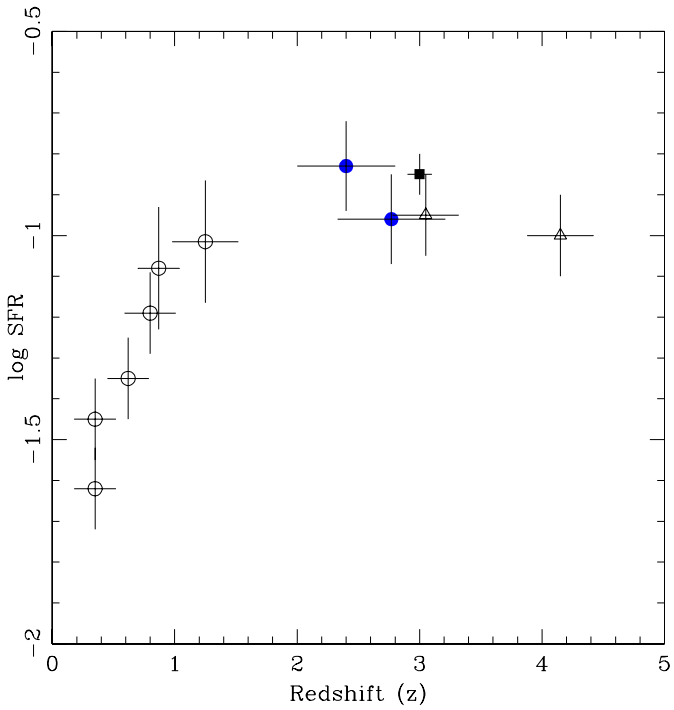

Fig. 9. Global star formation rate ($M_\odot$ yr^{-1} Mpc^{-3}) as a function of redshift, derived from complete spectroscopic surveys. Low redshift data ($z < 2$) are taken from Lilly et al. (1996) and Wilson et al. (2002). The higher redshift points (triangles) are from the $z = 3$ and $z = 4$ Lyman break galaxy samples of Steidel et al. (1999). The square symbol shows the X-ray estimate of the contribution to the global SFR from the $z \sim 3$ LBGs (Nandra et al. 2002). The filled circle at $z \sim 2.4$ shows our estimate of the contribution to the global SFR, derived from the high-z sample in the present work. The filled circle at $z \sim 2.8$ is the estimate obtained in the HDF-N sample.

In the first configuration the slits includes both the galaxy and the arc, while in the second only the galaxy falls in the slit. Unfortunately, better S/N spectra are needed to distinguish useful spectroscopic features and obtain a reliable redshift of the arc.

Since the arc is not a U-dropout, we can put an upper limit to its redshift of about 2.5, while a lower limit is provided by the redshift of the lensing galaxy, 0.577.

In the HDF-S there is an interesting radio source identified and discussed by Norris et al. (1999). This object ($ID = 373$) is unusual in that its radio-optical ratio is about 1000 times higher than that of any galaxy known in the local Universe. It has also been identified as an Extremely Red Object (ERO) with an $(I - Ks)_{AB} = 3.45$. In absence of strong emission lines the faintness of the object ($I_{AB} = 25.75$) has not allowed us to measure a spectroscopic redshift. The absence of strong emission lines, however, suggest that the photometric redshift estimated by Fontana et al. (2002), $z_{\rm phot} \sim 1.7$, is more likely than other, higher redshift possibilities (Norris et al. 1999).

Acknowledgements. We warmly thank A. Aragón-Salamanca, C. Chiosi, A. Renzini, P. van der Werf and S. White for stimulating the conception and the development of this work. This study has been conducted with partial support by the TMR program Formation and Evolution of Galaxies set up by the European Community under the contract FMRX-CT96-0086. This work was also partially supported by the ASI grants under the contract number ARS-98-226 and ARS-96-176, by the research contract of the University of Padova "The High redshift Universe: from HST and VLT to NGST" and by the Research Training Network "The Physics of the Intergalactic Medium" set up by the European Community under the contract HPRN-C12000-00126 RG29185. We also thank the referee for comments and suggestions that greatly improved the paper.

References

Arnouts, S., Cristiani, S., Moscardini, L., et al. 1999, MNRAS, 310, 540
Arnouts S., Moscardini, L., Vanzella, E., et al. 2002, MNRAS, 329, 355
Barkana, R., Hogg, D. W., Loeb, A., & Blandford, R. 2000 [astro-ph/0001325]
Bertin, E., & Arnouts, S. 1996, A&A, 117, 393
Bruzual, A. G., & Charlot, S. 1993, ApJ, 405, 538
Calzetti, D. 1997, AJ, 113, 162
Cohen, J. G., Hogg, D. W., Blandford, R., et al. 2000, ApJ, 538, 29 (C00, also [astro-ph/0012048])
Coleman, G. D., Wu, C. C., & Weedman, D. W. 1980, ApJS, 43, 393
Connolly, A. J., Csabai, I., Szalay, A. S., et al. 1995, AJ, 110, 2655
Cristiani, S., Appenzeller, I., Arnouts, S., et al. 2000, A&A, 359, 489
Cristiani, S., & D'Odorico, V. 2000, AJ, 120, 1648 (see http://www.stecf.org/hstprogrammes/J22/J22.html)
da Costa, L. N., et al. 1998, A&A, submitted [astro-ph/9812105]
Dennefeld, M. 2001, ESO observations of the Hubble Deep Field South, in Deep Fields, Proc. of the ESO Workshop 9–12 Oct. 2000, ed. S. Cristiani, A. Renzini, & R. Williams (Springer Verlag), 43

D'Odorico, V., Petitjean, P., & Cristiani, S. 2002, A&A, in press [astro-ph/0205299]
Fernández-Soto, A., Lanzetta, K. M., & Yahil, A. 1999, ApJ, 513, 34
Fontana, A., Menci, N., D'Odorico, S., et al. 1999, MNRAS, 310, L27
Fontana, A., D'Odorico, S., Poli, F., et al. 2000, AJ, 120, 2206
Fontana, A., Vanzella, E., Cristiani, S., et al. 2002, A&A, submitted
Franceschini, et al. 2002, in preparation
Madau, P., Ferguson, H. C., Dickinson, M. E., et al. 1996, MNRAS, 283, 1388
Lilly, S. J., Le Fevre, O., Hammer, F., & Crampton, D. 1996, ApJ, 460, L1
Meurer, G. R., Heckman, T. M., & Calzetti, D. 1999, ApJ, 521, 64
Nandra, K., Mushotzky, R. F., Arnaud, K., et al. 2002 [astro-ph/0205215]
Nicklas, H., Seifert, W., Boehnhardt, H., Kiesewetter-Koebinger, S., & Rupprecht, G. 1997, SPIE, 2871, 1222
Norris, R. P., Hopkins, A., Sault, R. J., et al. 1999, in Perspectives in Radio Astronomy: Science with Large Antenna Arrays, Proc. of the Conf. held at the Royal Netherlands Academy of Arts and Sciences in Amsterdam on 7–9 April 1999, ed. M. P. van Haarlem (ASTRON publisher, Dwingeloo), 101
Poli, F., Menci, N., Giallongo, E., et al. 2001, ApJ, 551, L45
Poli, F., Menci, N., Giallongo, E., et al. 2001, ApJ, 554, L127
Rigopoulou, D., Franceschini, A., Aussel, H., et al. 2000, ApJ, 537, L85
Saracco, P., Giallongo, E., Cristiani S., et al. 2001, A&A, 375, 1
Steidel, C. C., Adelberger, K. L., Giavalisco, M., Dickinson, M., & Pettini, M. 1999, ApJ, 519, 1
Vanzella, E., Cristiani, S., Saracco, P., et al. 2001, AJ, 122, 2190
Wang, Y., Bahcall, N., & Turner, E. L. 1998, AJ, 116, 2081
Wilson, G., Cowie, L. L., Barger, A. J., & Burke, D. J. 2002, AJ, submitted [astro-ph/0203168]